Comprehensive modeling of THz microscope with a sub-wavelength source

Hungyen Lin,* Christophe Fumeaux, Benjamin Seam Yu Ung, and Derek Abbott

School of Electrical & Electronic Engineering, The University of Adelaide, SA 5005, Australia

**hlin@eleceng.adelaide.edu.au*

Abstract: The sub-wavelength THz emission point on a nonlinear electro-optical crystal, used in broadband THz near-field emission microscopy, is computationally modeled as a radiating aperture of Gaussian intensity profile. This paper comprehensively studies the Gaussian aperture model in the THz near-field regime and validates the findings with dual-axis knife-edge experiments. Based on realistic parameter values, the model allows for THz beam characterisation in the near-field region for potential microscopy applications. An application example is demonstrated by scanning over a cyclic-olefin copolymer sample containing grooves placed sub-wavelengths apart. The nature of THz microscopy in the near-field is highly complex and traditionally based on experiments. The proposed validated numerical model therefore aids in the quantitative understanding of the performance parameters. Whilst in this paper we demonstrate the model on broadband electro-optical THz near-field emission microscopy, the model may apply without a loss of generality to other types of THz near-field focused beam techniques.

OCIS codes: (110.6795) Terahertz imaging; (300.6495) Spectrocsopy, terahertz; (110.0180) Microscopy; (180.4243) Near-field Microscopy.

References and links

1. P. H. Siegel, "Terahertz technology in biology and medicine," IEEE Trans. Microwave Theory Tech. **52**, 2438 – 2447 (2004).
2. M. Tonouchi, "Cutting edge terahertz technology," Nat. Photonics **1**, 97 – 105 (2007).
3. T. Yuan, J. Xu, and X.-C. Zhang, "Development of terahertz wave microscopes," Infrared Phys. Technol. **45**, 417 – 425 (2004).
4. W. Withayachumnankul, G. M. Png, X. Yin, S. Atakaramians, I. Jones, H. Lin, B. S. Y. Ung, J. Balakrishnan, B. W.-H. Ng, B. Ferguson, S. P. Mickan, B. M. Fischer, and D. Abbott, "T-ray sensing and imaging," Proceedings of the IEEE **95**, 1528 - 1558 (2007).
5. S. Hunsche, M. Koch, I. Brener, and M. Nuss, "THz near-field imaging," Opt. Commun. **150**, 22 – 26 (1998).
6. O. Mitrofanov, I. Brener, R. Harel, J. Wynn, L. Pfeiffer, K. West, and J. Federici, "Terahertz near-field microscopy based on a collection mode detector," Appl. Phys. Lett. **77**, 3496 – 3498 (2000).
7. O. Mitrofanov, I. Brener, M. Wanke, R. Ruel, J. Wynn, A. Bruce, and J. Federici, "Near-field microscope probe for far infrared time domain measurements," Appl. Phys. Lett. **77**, 591 – 593 (2000).
8. S. Mair, B. Gompf, and M. Dressel, "Spatial and spectral behavior of the optical near field studied by a terahertz near-field spectrometer," Appl. Phys. Lett. **84**, 1219 – 1221 (2004).
9. Y. Kawano, and K. Ishibashi, "An on-chip near-field terahertz probe and detector," Nat. Photonics **2**, 618 – 621 (2008).
10. N. van der Valk, and P. Planken, "Electro-optic detection of subwavelength terahertz spot sizes in the near field of a metal tip," Appl. Phys. Lett. **81**, 1558 – 1560 (2002).

#138468 - $15.00 USD Received 19 Nov 2010; revised 5 Jan 2011; accepted 9 Feb 2011; published 7 Mar 2011

11. K. Wang, A. Barkan, and D. Mittleman, "Sub-wavelength resolution using apertureless terahertz near-field microscopy," *CLEO*, CMP5 (2003).
12. H. T. Chen, R. Kersting, and G. C. Cho, "Terahertz imaging with nanometer resolution," Appl. Phys. Lett. **83**, 3009 – 3011 (2003).
13. T. Yuan, H. Park, J. Xu, H. Han, and X.-C. Zhang, "Field induced THz wave emission with nanometer resolution," Proc SPIE **5649**, 1 – 8 (2005).
14. A. J. Huber, F. Keilmann, J. Wittborn, J. Aizpurua, and R. Hillenbrand, "Terahertz near-field nanoscopy of mobile carriers in single semiconductor nanodevices," Nano Letters **8**, 3766 – 3770 (2008).
15. R. Kersting, F. Buersgens, G. Acuna, and G. Cho, "Terahertz near-field microscopy," *Advances in Solid State Physics* (Springer Berlin / Heidelberg, 2008).
16. H. G. von Ribbeck, M. Brehm, D. W. van der Weide, S. Winnerl, O. Drachenko, M. Helm, and F. Keilmann, "Spectroscopic THz near-field microscope," Opt. Express **16**, 3430 – 3438 (2008).
17. M. Wächter, M. Nagel, and H. Kurz, "Tapered photoconductive terahertz field probe tip with subwavelength spatial resolution," Appl. Phys. Lett. **95**, 041112 (2009).
18. K. Wynne, and D. Jaroszynski, "Superluminal terahertz pulses," Opt. Lett. **24**, 25 – 27 (1999).
19. Q. Chen, Z. Jiang, G. Xu, and X.-C. Zhang, "Near-field terahertz imaging with a dynamic aperture," Opt. Express **25**, 1122 – 1124 (2000).
20. T. Yuan, S. P. Mickan, J. Xu, D. Abbott, and X.-C. Zhang "Towards an apertureless electro-optic T-ray microscope," *CLEO*, 637 – 638 (2002).
21. T. Kiwa, M. Tonouchi, M. Yamashita, and K. Kawase, "Laser terahertz-emission microscope for inspecting electrical faults in integrated circuits," Opt. Lett. **28**, 2058 – 2060 (2003).
22. A. J. L. Adam, J. M. Brok, M. A Seo, K. J. Ahn, D. S. Kim, J. H. Kang, Q. H. Park, M. Nagel, and P. C. Planken, "Advanced terahertz electric near-field measurements at sub-wavelength diameter metallic apertures," Opt. Express **16**, 7407 – 7417 (2008).
23. A. Bitzer, and M. Walther, "Terahertz near-field imaging of metallic subwavelength holes and hole arrays," Appl. Phys. Lett. **92**, 231101 (2008).
24. R. Lecaque, S. Gresillon, and C. Boccara, "THz emission Microscopy with sub-wavelength broadband source," Opt. Express **16**, 4731 – 4738 (2008).
25. T. Kiwa, Y. Kondo, Y. Minami, I. Kawayama, M. Tonouchi, and K. Tsukada, "Terahertz chemical microscope for label-free detection of protein complex," Appl. Phys. Lett. **96**, 211114 (2010).
26. H. Lin, C. Fumeaux, B. M. Fischer, and D. Abbott, "Modelling of sub-wavelength THz sources as gaussian apertures," Opt. Express **18**, 17672 – 17683 (2010).
27. J. Xu, and X.-C. Zhang, "Optical rectification in an area with a diameter comparable to or smaller than the center wavelength of terahertz radiation," Opt. Lett. **27**, 1067 – 1069 (1999).
28. G. Dakovski, B. Kubera, and J. Shan, "Localized terahertz generation via optical rectification in ZnTe," J. Opt. Soc. Am. B **22**, 1667 – 1670 (2005).
29. Y. S. Lee, *Principles of Terahertz Science and Technology* (Springer, New York, USA, 2008).
30. B. E. A. Saleh, and M. C. Teich, *Fundamentals of Photonics* (John Wiley & Sons, 1991).
31. M. I. Bakunov, S. B. Bodrov, and A. V. Maslov, "Temporal Dynamics of Optical-to-Terahertz Conversion in Electro-Optic Crystal," *CLEO*, JWA93 (2007).
32. P. Bonnet, X. Ferrieres, B. L. Michielsen, P. Klotz, and J. L. Roumiguières, *Finite-volume time domain method, in Time Domain Electromagnetics* (S. M. Rao, Ed. San Diego, CA: Academic Press, 1999).
33. D. Baumann, C. Fumeaux, C. Hafner, E.P. Li, "A modular implementation of dispersive materials for time-domain simulations with application to gold nanospheres at optical frequencies," Opt. Express **17**, 15186 – 15200 (2009).
34. C. Fumeaux, D. Baumann, S. Atakaramians, and E. Li, "Considerations on paraxial Gaussian beam source conditions for time-domain full-wave simulations," *25th Annual Review of Progress in Applied Computational Electromagnetics*, 401 – 406 (2009).
35. A. Taflove, and S. C. Hagness, *Computational Electrodynamics: The Finite-Difference Time-Domain Method* (Artech House, 2005).
36. C. Fumeaux, D. Baumann, P. Leuchtmann, R. Vahldieck, "A generalized local time-step scheme for efficient FVTD simulations in strongly inhomogeneous meshes," IEEE Trans. Microwave Theory Tech. **52**, 1067 – 1076 (2004).
37. C. Fumeaux, K. Sankaran, R. Vahldieck, "Spherical perfectly matched absorber for finite-volume 3-D domain truncation," IEEE Trans. Microwave Theory Tech. **55**, 2773 – 2781 (2007).
38. B. M. Fischer, "Broadband THz Time-Domain Spectroscopy of Biomolecules," *Ph.D. Thesis, University of Freiburg* (2005).
39. H. Lin, B. M. Fischer, and D. Abbott "Comparative simulation study of ZnTe heating effects in focused THz radiation generation," *35th International Conference on Infrared, Millimeter, and Terahertz Waves*, 63 – 64 (2010).

#138468 - $15.00 USD Received 19 Nov 2010; revised 5 Jan 2011; accepted 9 Feb 2011; published 7 Mar 2011

1. Introduction

Terahertz imaging offers many attractive advantages over existing imaging modalities especially in its ability to obtain spectroscopic information [1, 2]. However, one of the major limitations of THz imaging is low spatial resolution, as determined by Rayleigh's criterion with a wavelength at 300 μm (for 1 THz). The general motivation behind an increased resolution is to distinguish objects in close proximity and to cater for a smaller sample size. The resolution of THz far-field imaging is in the sub-millimeter range and therefore insufficient for potential future imaging applications such as biological cells (micron to sub-micron range) and microstructures in semiconductor structures (sub-micron to nanometer range). Extensive reviews on pulsed THz near-field imaging techniques have been published [3, 4]. The techniques in general can be categorised as aperture, tip, and highly focused-beam approaches. Aperture based approaches [5–9] require physical sub-wavelength apertures where the spatial resolution is dependent on the aperture size, but no longer on the wavelength. However, the sub-wavelength nature of the aperture places a limitation on the radiation throughput leading to a deterioration in the Signal-to-Noise Ratio (SNR). Finite thickness of the aperture also exhibits waveguide effects that attenuates evanescent low-frequency components and makes detection difficult. Metallic tip based approaches [10–17] have to date demonstrated the highest resolution down to the nanometer range. The approach, however, is complicated with the introduction of a near-field tip, and suffers from low output power. Furthermore, some of the presented techniques are only valid for semiconductor samples. Focused-beam techniques exploit the micron sized far-infrared pump or probe beam spot for generating or detecting THz radiation respectively to achieve sub-wavelength resolution [18–25]. The approach is comparatively simpler and does not heavily rely on micro-fabrication technologies. These sub-wavelength THz sources have been investigated in the far-field regime as a radiating aperture of Gaussian profile [26], using semi-analytical techniques commonly applied at microwave frequencies. The results of that investigation helped in explaining the far-field experimental observations reported in [27, 28]. The techniques presented are however only applicable for far-field interactions and far-field detection, and therefore, are unsuitable for interpreting the effect in the more complicated near-field regime. Motivated by an increasing interest in the focused-beam THz near-field microscopy technique, the present paper provides a numerical approach to accurately characterize electro-optically generated THz radiation in the near-field. The numerical results based on a radiating Gaussian aperture source are validated experimentally, and a practical application of the model to extrapolate the THz beam spot to infer system resolution is also demonstrated.

2. Experimental near-field beam characterization

A THz hybrid setup that generates THz radiation by optical rectification and detection via a Photoconductive Antenna (PCA) is used in our experiment, as shown in the setup in [26]. An average infrared (IR) pump power of 30 mW is used for THz radiation generation with a 1 mm thick $\langle 110 \rangle$ ZnTe crystal from Zomega Terahertz Corporation. An optical lens of 200 mm focal length is used to focus down the IR pump beam to a waist of 51 μm with a Rayleigh range of 10 mm. Taking into consideration the beam divergence in the crystal, the effective IR pump beam waist is expected to be slightly larger than the theoretical value. An approximate maximal SNR of 40 dB and a bandwidth of more than 2.5 THz is achieved [26]. A dual-axis (i.e. x and y-axis) knife-edge profile measurement is conducted on the generated THz beam at a distance of 150 μm, as determined from the tip of the knife-edge to the crystal surface. The minimal possible near-field distance is constrained in this case by the razor blades' thickness. This distance is measured with a CCD camera in the actual experiment. A dual-axis knife edge profile is necessary for a thorough THz beam characterization in the near-field because the radial symmetry of the polarized THz beam is broken at the air-crystal interface.

#138468 - $15.00 USD Received 19 Nov 2010; revised 5 Jan 2011; accepted 9 Feb 2011; published 7 Mar 2011

Even though the appropriate crystal to knife-edge distance cannot be achieved simultaneously for both axes, a two knife system as shown in Fig. 1 is realized to minimize experimental uncertainties. Sheffield steel razor blades are used as knife-edges.

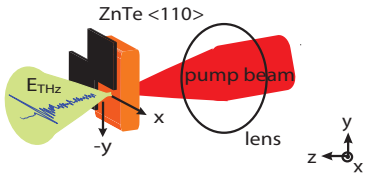

Fig. 1. The pump laser beam is focused into a 1 mm thick ZnTe crystal by means of an optical lens. The emitted THz radiation polarized parallel to the *x*-axis is sliced along the *x*-axis and *y*-axis respectively by translating two sharp razor blades in the near-field region in parallel to the crystal back surface.

3. Modeling of the THz knife-edge experiment

The following sections describe the electromagnetic modeling of the full knife-edge experiment from electro-optical beam generation to detection. The model combines several techniques and requires simplifications to become tractable in terms of complexity and computational effort. Modeling the knife-edge experiment and comparing the results to experimental data provides a validation of the general simulation approach.

3.1. Sub-wavelength THz source

The generation of THz radiation with optical rectification in a nonlinear crystal is a square-law process [29]. The pump beam is typically a Gaussian IR beam, i.e. can be approximated as a solution to the paraxial wave equation characterised by a Gaussian intensity distribution in any plane transverse to the direction of propagation [30]. The coherent generation of THz radiation in the ZnTe electro-optical crystal is then a source with Gaussian profile distributed along the optical beam axis. The square relationship between generated THz electric field to the optical electric field therefore implies a reduction factor of $\sqrt{2}$ in the radius of THz source. In the present model, the THz source is approximated as the radiation from an aperture with a Gaussian intensity profile, located inside the crystal. This type of Gaussian aperture is similar as introduced in [26] for investigation of the far-field THz radiation. This simplified approach could be in principle refined by using as source an aperture field distribution based on analytical modelling of the nonlinear effects a presented in [31]. Alternatively, for thick crystals, a model comprising a series of aperture sources distributed along the z-axis could be applied in modeling distributed THz generation along the crystal.

3.2. Full-wave near-field electromagnetic simulation

In the present study, the Gaussian aperture source is placed inside the crystal surface and the near-field wave propagation is simulated with a electromagnetic simulation tool based on the Finite-Volume Time-Domain (FVTD) method [32, 33]. The application of in-house developed code is motivated by the possibility of implementing a sub-wavelength Gaussian aperture source as demonstrated in [34]. This flexibility in implementation is not readily available in most commercial software, even if other full-wave simulation methods such as the Finite-Difference Time-Domain method [35] would in principle be appropriate for simulation. The FVTD model is shown in Fig. 2. The Gaussian aperture source plane is displaced inside the crystal, 300 μm away from the output surface. A metallic knife-edge is scanned through the

#138468 - $15.00 USD Received 19 Nov 2010; revised 5 Jan 2011; accepted 9 Feb 2011; published 7 Mar 2011

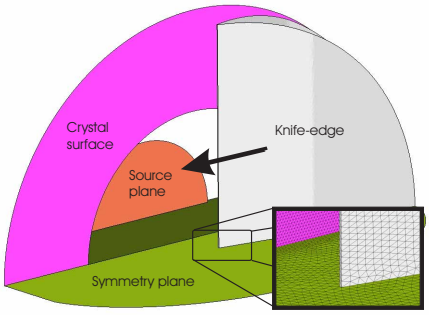

Fig. 2. Schematic of the numerical FVTD model. The center of the crystal surface is opened up in its center to reveal the source plane inside of the EO crystal. The inset shows the surface skin triangulation and illustrates the refinement of the mesh near the blade tip and on the crystal surface.

beam in a series of simulations, mimicking the experimental beam characterization. The knife-edge has a thickness of 150 μm and is scanned parallel to the crystal surface at a fixed distance of 150 μm between its tip and the crystal surface. The blade tip is tapered at an approximate angle of 21° as observed from CCD images, and the tip end is flattened to mimic a realistic finite tip sharp width of 4 μm. A symmetry plane is introduced to halve the computational domain size. The nature of this symmetry plane depends on the knife-edge slice considered, i.e. scanning along the *x* or *y*-axis in Fig. 1, which corresponds to the two orthogonal polarizations in the computational model. For the *y*-axis scan, the electric field is perpendicular to the symmetry plane leading to a perfect electric conductor (PEC). Analogously, the symmetry plane is a perfect magnetic conductor (PMC) in the *x*-axis scan. The volume is discretized with an inhomogeneous tetrahedron mesh [36] to resolve the geometry near the fine tip, and to refine the discretization in the crystal with a relative permittivity of ε_r of 9. The computational domain is subsequently truncated with a perfectly matched absorber [37]. The Gaussian sub-wavelength source is excited with a sine-modulated Gaussian pulse, which covers the frequency spectrum from 300 GHz to 2.5 THz. The computational cost is relatively heavy considering the size of the computational domain in terms of wavelength, and the fact that a simulation has to be performed sequentially for each position of the blade. Also at every blade position, discrete Fourier transformation are performed on the fly during the time iteration of the FVTD simulation to obtain the equivalent frequency representations. Figures 3 and 4 illustrate the THz electric field amplitude for the *x*-axis and *y*-axis knife-edge with the tip positioned at the center of the beam for selected low and high frequencies respectively. The images show a standing-wave pattern inside of the crystal because of the reflection at the output surface. The dielectric interface breaks the radial symmetry of the beam, as the refraction is polarization-dependent. The figures further illustrate the polarization dependent diffraction from the knife-edge tip.

3.3. Near-field to far-field transformation

The full-field simulation can only describe wave propagation and material interactions in a very limited volume close to the source. Therefore, a discrete implementation of the frequency-domain near-to-far-field transformation is performed in accordance with [35] to simulate the radiation pattern relevant for far-field detection. The surface where the equivalent currents are sampled (Hugyens' surface) is chosen as a flat plane located after the knife-edge. Figures 5

#138468 - $15.00 USD Received 19 Nov 2010; revised 5 Jan 2011; accepted 9 Feb 2011; published 7 Mar 2011

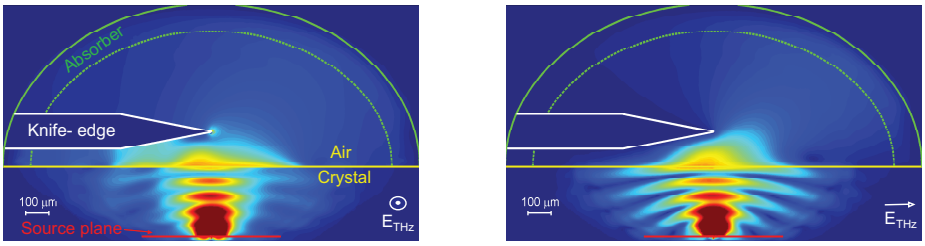

(a) (b)

Fig. 3. Amplitude distribution at 0.8 THz with a simulated (a) *x*-axis and (b) *y*-axis knife-edge.

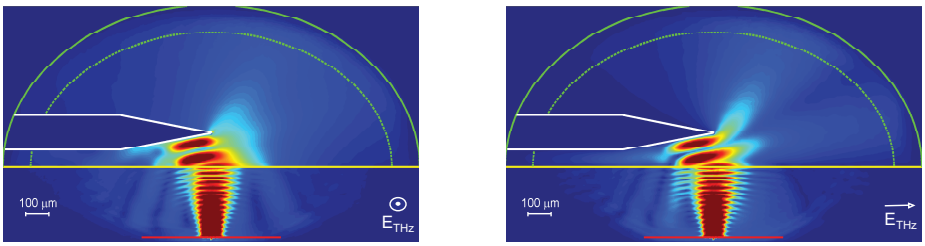

(a) (b)

Fig. 4. Amplitude distribution at 2.4 THz with a simulated (a) *x*-axis and (b) *y*-axis knife-edge.

show the obtained amplitude radiation patterns at 0.8 and 2.4 THz respectively. The nature of the THz Time Domain Spectroscopy (TDS) detection setup constrains the angle of acceptance at the first parabolic mirror for the power guided to the detector. The green dashed lines on the radiation patterns therefore delimit this acceptance angle of 28°. Effects of aberration, diffraction and propagation losses through the rest of the optical detection path are assumed to be negligible.

3.4. Detection modeling

In our modeled knife-edge experiment, the power available for detection is not the total radiated power that passes the knife-edge, but only the power integrated in the mentioned acceptance angle from the crystal to the parabolic mirror about the axis of optical propagation. To mimic the THz detection by the antenna located in a typical TDS detection setup, the far-field power has to be integrated coherently in the acceptance angle, e.g. taking into account both amplitude and phase patterns.

4. Results and discussion

4.1. Experimental results

Fourier transforms of the experimentally acquired THz time-domain waveforms are computed and the amplitude at each extracted frequency is plotted against the position of the knife-edge for the respective axes. For the sake of simplicity, only the power spectrum at a certain knife-edge location and the knife-edge of selected frequency components in this study are shown in Fig. 6 and 7 for *x* and *y*-axis respectively. As the experiment is conducted in low humidity atmosphere, the frequency components selected are unaffected by water vapor absorption and

#138468 - $15.00 USD Received 19 Nov 2010; revised 5 Jan 2011; accepted 9 Feb 2011; published 7 Mar 2011

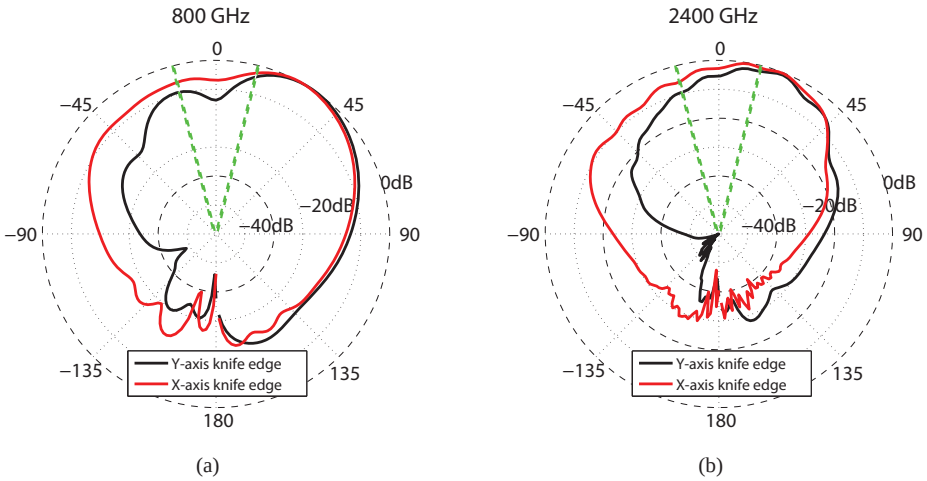

(a) (b)

Fig. 5. Normalized THz amplitude radiation pattern with the *x*-axis and *y*-axis knife edge at the center of the beam for frequencies (a) 0.8 THz and (b) 2.4 THz. The green dashed lines highlight the acceptance angle of 28° from the crystal to the parabolic mirror, within which the THz radiation is measured.

noise that occur at high THz frequencies. A one step running average over two points has been used to preserve data integrity. The *y*-axis knife-edge profile shows a stronger diffraction over the *x*-axis as imposed by the boundary conditions from having the knife-edge parallel to the THz electric field.

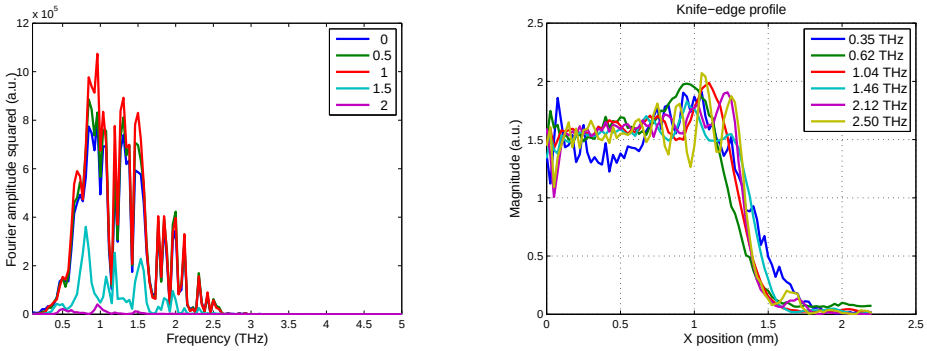

(a) (b)

Fig. 6. (a) The power spectrum of the THz waveforms acquired with a *x*-axis knife-edge scanned at a distance of 150 μm from the crystal. With each movement of the knife, the THz electric field becomes weaker until when the THz radiation is entirely blocked by the knife. This can be seen at x = 0 mm, where the knife does not obstruct the THz beam, as opposed to x = 2 mm, where the THz radiation is totally blocked. (b) Selected frequency components are shown at different knife positions.

#138468 - $15.00 USD Received 19 Nov 2010; revised 5 Jan 2011; accepted 9 Feb 2011; published 7 Mar 2011

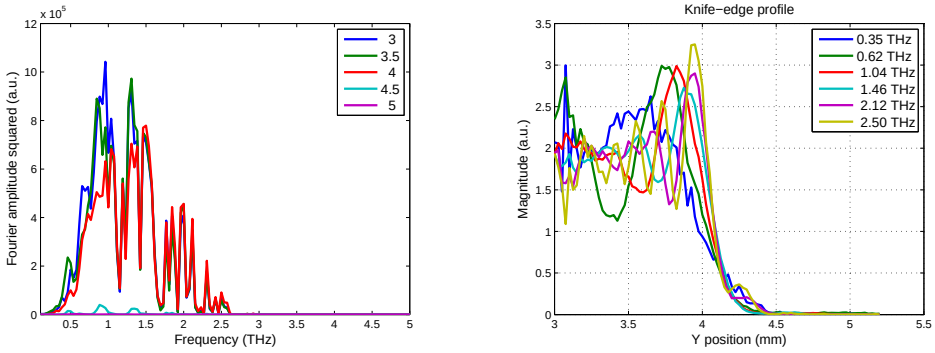

(a) (b)

Fig. 7. (a) The power spectrum of the THz waveforms acquired with a *y*-axis knife-edge scanned at a distance of 150 μm from the crystal. With each movement of the knife, the THz field becomes weaker until when the THz radiation is entirely blocked by the knife. This can be seen at y = 3 mm, where the knife does not obstruct the THz beam, as opposed to y = 5 mm, where the THz radiation is totally blocked. (b) Selected frequency components are shown at different knife positions.

4.2. Model validation

In order to validate the developed Gaussian aperture numerical model, the experimental setup is simulated with the estimated and measured values for experimental parameters like (i) IR pump beam waist, (ii) acceptance angle as determined from the crystal-parabolic distance at the parabolic mirror focal point, (iii) knife to crystal surface distance and (iv) the THz frequency of interest. The exact IR pump beam waist inside the crystal is estimated to be 51 μm from the optical setup. The Gaussian profile of the generated THz beam is proportional to the IR power, i.e. the waist will be reduced by a factor of $\sqrt{2}$ to 36 μm. In reality, THz radiation generation is distributed along the bulk crystal thickness, but in our model, the distributed THz radiation generation is approximated as an aperture located at an effective distance (300 μm) within the crystal. Figures 8 to 13 show the simulated and experimental *x*-axis and *y*-axis knife-edge profiles at selected frequencies. The simulation is normalized with respect to the full power, while the measurement is normalized for best visual fit because measurement does not clearly yield the full power. The sensitivity of the system modeling to this parameter is probed by altering this distance to 100 μm and negligible qualitative changes in the final results are observed. The simulated knife-edges closely matches all the experimental results in terms of the integral function shape and slope. Qualitatively, diffraction effects in the simulated knife-edge profiles appear to be coincide well with the measured results. Differences are attributed to the discrepancy between the modeled and physical shape of the blade tip. With the beam waist or aperture size held constant, it is noteworthy to observe the changes in the THz beam waist as the frequency increases. At low frequencies (0.35 THz), the knife-edge profiles have a small slope implying a relatively large THz beam waist. This frequency range corresponds to the regime where the far-field radiation pattern resembles that of an obliquity factor in the far-field [26]. At higher frequencies (0.615 THz and 1.04 THz), the slopes begins to increase consistently with the increase of aperture size relatively to the wavelength. The overall agreement between the modeled and the experimental knife-edge characterization is validating the modeling procedure. The decrease in beam waist with increasing frequency is well described quantitatively by the simulations, while the diffraction effects that are strongly dependent on the actual dimensions

#138468 - $15.00 USD Received 19 Nov 2010; revised 5 Jan 2011; accepted 9 Feb 2011; published 7 Mar 2011

of the blade are demonstrated qualitatively.

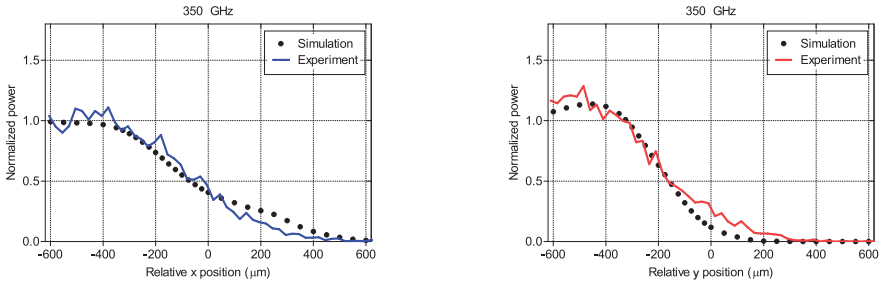

(a) (b)

Fig. 8. (a) *x*-axis and (b) *y*-axis experimental and simulated knife-edge profile of THz radiation beam at 150 μm from the crystal backside at 0.35 THz.

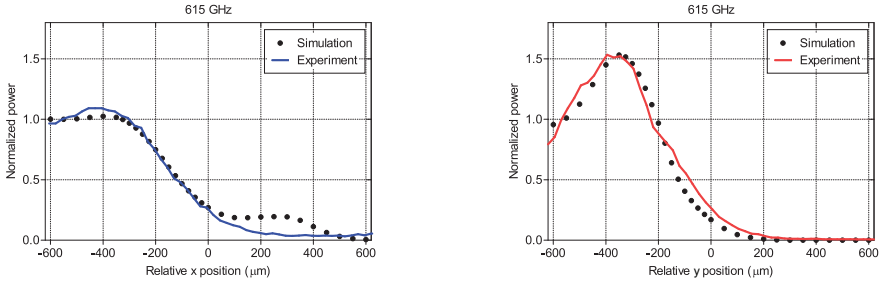

(a) (b)

Fig. 9. (a) *x*-axis and (b) *y*-axis experimental and simulated knife-edge profile of THz radiation beam at 150 μm from the crystal backside at 0.615 THz.

5. THz microscopy application

The intent of near-field studies is to resolve small samples that are a sub-wavelength distance apart. To demonstrate an application of the computational model, the validated model can be used to predict the THz beam profile of selected frequencies at a near-field distances of 50 μm from the crystal emitting surfaces as shown in Fig. 14. Vertical structures with decreasing sub-wavelength separation distance are simulated by a groove function as illustrated in the left column of Fig. 15(a). Convolving the simulated THz beam profile (electric field distribution) with the decreasing grooves separation distances in the groove function yields the imaging capability. Note, however, convolution does not take diffraction into account that is present in real scans. The system response to convolution predicts the resolving of the grooves at 1.26 THz and above as can be seen in the left column of Fig. 15(b)-(d). For experimental verification, a cyclic-olefin copolymer (TOPAS) sample comprising of identical vertical grooves is fabricated and scanned with the THz near-field microscope at an identical distance of 50 μm from crystal surface. The vertical structure of the grooves ensures that only scans along *x*-axis is required. This minimizes the typically long scanning time associated with two-dimensional THz pixel-by-pixel imaging. Optical constants of TOPAS in the THz region as a function of frequency as measured in THz-TDS can be found in [38]. A groove depth of 50 μm ensures it is

#138468 - $15.00 USD Received 19 Nov 2010; revised 5 Jan 2011; accepted 9 Feb 2011; published 7 Mar 2011

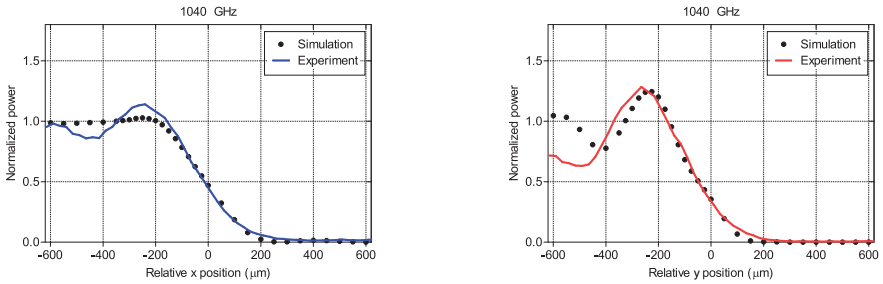

(a) (b)

Fig. 10. (a) *x*-axis and (b) *y*-axis experimental and simulated knife-edge profile of THz radiation beam at 150 μm from the crystal backside at 1.04 THz.

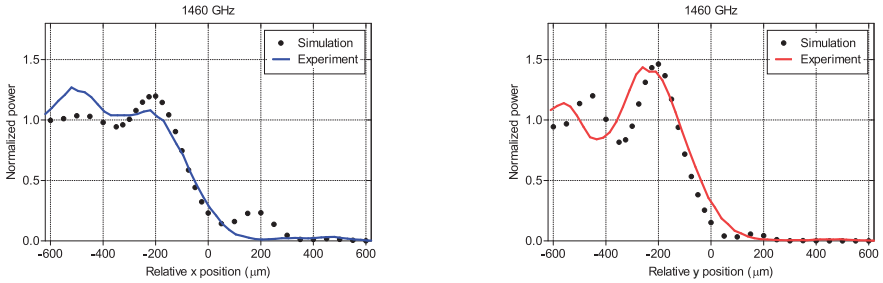

(a) (b)

Fig. 11. (a) *x*-axis and (b) *y*-axis experimental and simulated knife-edge profile of THz radiation beam at 150 μm from the crystal backside at 1.46 THz.

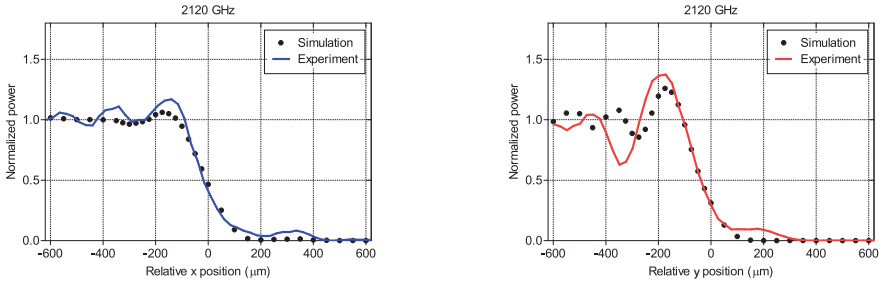

(a) (b)

Fig. 12. (a) *x*-axis and (b) *y*-axis experimental and simulated knife-edge profile of THz radiation beam at 150 μm from the crystal backside at 2.1 THz.

#138468 - $15.00 USD Received 19 Nov 2010; revised 5 Jan 2011; accepted 9 Feb 2011; published 7 Mar 2011

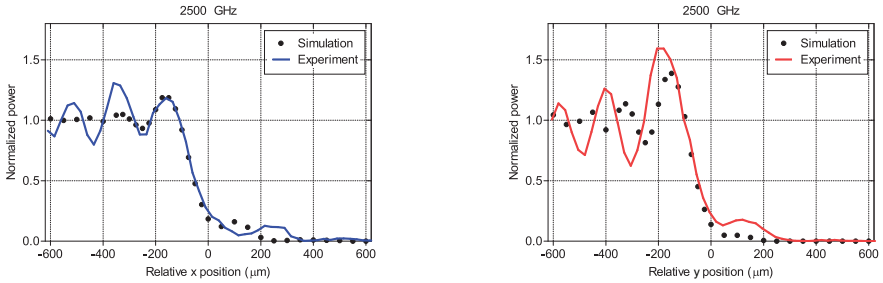

Fig. 13. (a) *x*-axis and (b) *y*-axis experimental and simulated knife-edge profile of THz radiation beam at 150 μm from the crystal backside at 2.5 THz.

within the THz source near-field region as considered from the output surface from the crystal, and the grooves width effectively dictate the sample size. A photo of the optically transparent sample on a black background is shown in right column of Fig. 15(a), with the grooves in gray. Figures 15(b)-(d) show the grayscale image of the amplitude component of the selected frequencies. Bright regions indicate a high amplitude caused by diffraction as opposed to the dark regions that represent the low amplitudes. Resolving a separation distance of 100 μm with 1.26 THz confirms sub-wavelength resolution of smaller than $\lambda/2.3$. This is in close qualitative agreement with the extrapolated results in the left column.

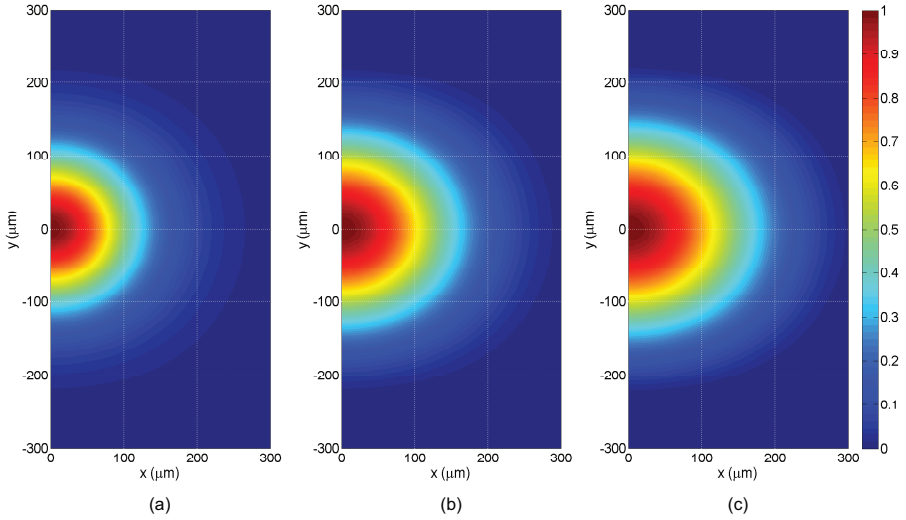

Fig. 14. Contour plot along the *x* and *y*-axis of the THz beam profile at 50 μm away from crystal surface at (a) 2 THz (b) 1.26 THz and (c) 1 THz. The normalized *z*-component of the Poynting vector is represented.

6. Conclusion

In this paper we have computationally modeled the sub-wavelength THz emission point on a nonlinear electro-optical crystal, used in broadband THz near-field emission microscopy, as a radiating aperture with Gaussian intensity distribution. We have validated the model of

#138468 - $15.00 USD Received 19 Nov 2010; revised 5 Jan 2011; accepted 9 Feb 2011; published 7 Mar 2011

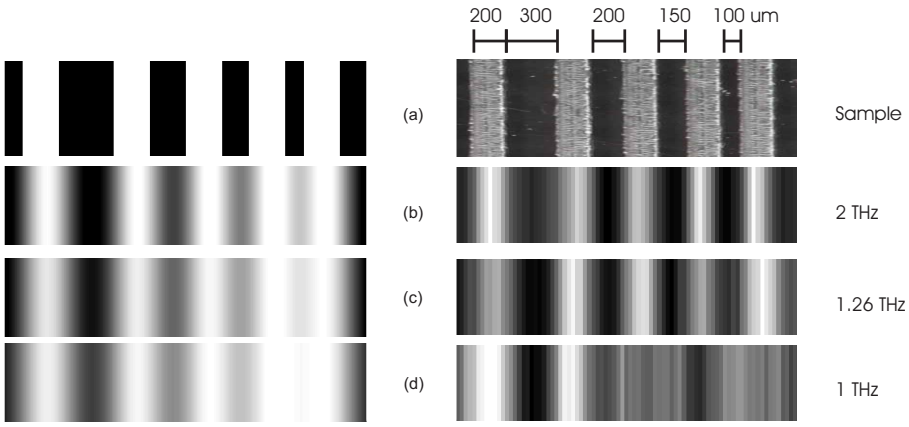

Fig. 15. (a) (Left) Simulated sample structure comprising of grooves separated by decreasing sub-wavelength distances. (Right) The TOPAS sample comprising of vertical grooves (in white) separated by sub-wavelength distances of 300 μm, 200 μm, 150 μm and 100 μm. (b) (Left) Response from convolving THz beam waist at 2 THz with the simulated sample. (Right) Experimental grayscale image of the magnitude at 2 THz, resolves all distances. (c) (Left) Response from convolving THz beam waist at 1.26 THz with the simulated sample. (Right) Experimental grayscale image of the magnitude at 1.26 THz, resolves all distances. (d) (Left) Response from convolving THz beam waist at 1 THz with the simulated sample. (Right) Experimental grayscale image of the magnitude at 1 THz, resolves only the 300 μm distance.

the Gaussian aperture by inserting dual-axis experimental knife-edges in the near-field region while taking into account the limitation of THz radiation detection setup. An application example is demonstrated by scanning over a fabricated cyclic-olefin copolymer sample, embedded with grooves sub-wavelengths apart, and a resolution of smaller than $\lambda/2.3$ is achieved in accordance with the model. As a whole, the model aids in the quantitative understanding of the many trade-offs between parameters, such as optical beam waist, crystal sample distance and frequency components, critical to this type of THz near-field microscope design. A micron-sized resolution for biological microscopy is achievable by means of a smaller aperture realized by tighter focusing of the IR pump beam and a shorter detection setup distance. This in turn implies a smaller Rayleigh range and hence requires a crystal tens of microns thick. As the generated THz electric field is proportional to the crystal length and that prolonged exposure leads to heating effects [39], future work aims to incorporate crystal length and hence the generated THz power into the numerical model. The work has introduced and validated numerical techniques for the 3D modeling of a focused beam THz near-field setup with electro-optical crystal and can be extended without a loss of generality to other focused beam THz techniques.

Acknowledgments

The authors gratefully acknowledge Dr Withawat Withayachumnankul for useful discussions during the course of this work and workshop staff Mr Ian Linke and Mr Alban O'Brien. This project is funded by the Australian Research Council (ARC) project number DP09888673.

#138468 - $15.00 USD Received 19 Nov 2010; revised 5 Jan 2011; accepted 9 Feb 2011; published 7 Mar 2011